https://doi.org/10.21608/sjsci.2025.425258.1312

# Green synthesis of Co<sub>3</sub>O<sub>4</sub> NPs via microwave approach: Enhanced H<sub>2</sub> generation from NaBH<sub>4</sub> hydrolysis

Simon W. Samouel<sup>1</sup>, Tarek T. Ali <sup>1,\*</sup>, Bahaa M. Abu-Zied <sup>2</sup>, Hatem A. Mahmoud <sup>1,\*</sup>

<sup>1</sup>Chemistry Department, Faculty of Science, Sohag University, Sohag 82524, Egypt

<sup>2</sup>Chemistry Department, Faculty of Science, Assiut University, 71516 Assiut, Egypt

\*Email: <u>sjs@science.sohag.edu.eg</u>

Received: 19th Septamber 2025 Revised: 16th October 2025 Accepted: 22nd October 2025

Published online: 15th November 2025

Abstract: This study employed parsley leaves in the green synthesis of cobalt oxide ( $Co_3O_4$ ) nanoparticles (NPs) using a microwave irradiation approach and subsequent calcination at 400 °C. The synthesized  $Co_3O_4$  NPs have been characterized through various analyses including XRD, FTIR, TEM, XPS, and  $N_2$  adsorption. XRD analysis revealed the cubic structure of the formed  $Co_3O_4$  NPs, with an average crystallite size of 15 nm. Functional groups were identified from FT-IR analysis which confirmed the presence of the two diagnostic peaks corresponding to  $Co^{2+}$  and  $Co^{3+}$  of  $Co_3O_4$  spinel. TEM images demonstrated that the synthesized  $Co_3O_4$  NPs possess agglomerated nanoparticles, which exhibit capsule-like morphology with an average particle size of 10 nm. Surface analysis via  $N_2$  adsorption indicated that the catalyst has a high surface area ( $S_{BET}$ ) value of 90 m<sup>2</sup>g<sup>-1</sup>. XPS characterization of these NPs confirmed the coexistence of  $Co^{2+}$  and  $Co^{3+}$  at the surface of the synthesized  $Co_3O_4$  NPs. The catalytic activity of the synthesized catalyst was assessed for the hydrolysis of NaBH<sub>4</sub> at temperatures ranging from 30 to 45 °C. The catalytic performance increased with the increase in reaction temperature, NaBH<sub>4</sub> wt.%, and catalyst weight. Moreover, the investigation was extended to explore the effect of other parameters including alkalinity and reusability on the catalyst's activity.

Keywords: Hydrogen generation, Co<sub>3</sub>O<sub>4</sub> NPs, microwave method, NaBH<sub>4</sub> hydrolysis, and parsley leaves.

#### 1. Introduction

Recently, scientific research has demonstrated a trend toward developing various green methods for synthesizing materials, especially nanoparticles, which enhance the safety and ecological sustainability of the synthetic process. Moreover, the distinctive chemical composition of biological systems enables nanoparticles produced by these processes to have unique structural and physicochemical properties [1, 2]. The application of oxide NPs has received significant attention due to their unique properties, such as extremely tiny size, high surface area-to-volume ratio, surface modification, beneficial magnetic properties, and biocompatibility. Among the diverse oxide NPs, cobalt exists in multiple oxidation states, including cobaltous oxide (CoO), cobaltic oxide (Co<sub>2</sub>O<sub>3</sub>), and cobaltosic oxide (Co<sub>3</sub>O<sub>4</sub>), which represent the principal category of cobaltbased NPs in varying oxidation states. Co<sub>3</sub>O<sub>4</sub> (CoCo<sub>2</sub>O<sub>4</sub>) NPs comprise cobalt ions in two oxidation states, viz. Co2+ ions located at tetrahedral sites and Co<sup>3+</sup> ions at octahedral ones.

Co<sub>3</sub>O<sub>4</sub> NPs are employed in several applications including gas sensors, pigments, catalysts, magnetic materials, electronic devices, anode materials for rechargeable batteries, high-temperature solar selective absorbers, solar energy system magnetic devices, and biological applications, such as cancer therapies [3, 4]. Therefore, a variety of methods have been utilized to synthesize Co<sub>3</sub>O<sub>4</sub> NPs, including hydrothermal [5], sol-gel [6], precipitation [7], thermal decomposition [8], microwave-assisted [9], and solution combustion [10].

High-catalytic activity is demonstrated by Co<sub>3</sub>O<sub>4</sub> NPs in the oxidation of carbon monoxide [11], the catalytic decomposition

of nitrous oxide [12], hydrolysis of sodium borohydride [10]. The catalytic hydrolysis of sodium borohydride is an effective and affordable operating approach with significant promise as an alternative for fossil fuels is to generate hydrogen [13]. In the meantime, most of the hydrogen generated globally is derived from fossil fuels through processes such as steam reforming of natural gas, coal gasification, pyrolysis of hydrocarbons, partial oxidation of methane, and water electrolysis [14]. The utilization of fossil fuels possesses environmental issues and concerns regarding non-renewability, whereas water hydrolysis faces challenges related to the conversion of one energy form into another. These considerations impede hydrogen production as a sustainable and clean fuel source. Hydrogen is widely acknowledged as an essential component of the global transition to clean, sustainable energy sources. Hydrogen, a clean-burning fuel with a high energy density, has the potential to generate power for wide spectrum of energy consuming supplements from vehicles to stationary generators. Despite the potential of hydrogen energy, its widespread application remains limited.

In recent years, there has been more attention placed on hydrogen production through the hydrolysis of metal hydrides, owing to their controllability, safety, and high theoretical hydrogen yield. There are various forms of hydrogen storage materials such as chemical hydrides (NaBH<sub>4</sub>, LiBH<sub>4</sub>, NH<sub>3</sub>BH<sub>3</sub>, KBH<sub>4</sub>) [15]. Among the several approaches for hydrogen generation, the hydrolysis of sodium borohydride (NaBH<sub>4</sub>) has been investigated as a promising route to meet the growing need for clean energy while reducing environmental issues. This procedure provides several advantages, including safety, a high hydrogen storage capacity of 10.8 wt.%, stability in alkaline

# **Research Article**

solutions, non-toxic by-products, and pure hydrogen generation [16]. Hydrolysis of NaBH<sub>4</sub> reaction includes its reaction with water, which leads to the liberation of hydrogen gas and the formation of sodium metaborate (NaBO<sub>2</sub>) as a byproduct. This hydrolysis happens exothermically at ambient temperature [17]. The reaction can be declared as follows:

 $NaBH_{4(aq)} + 2H_2O_{(aq)} \rightarrow NaBO_{2(aq)} + 4H_{2(g)} \uparrow$  Eq. 1

During hydrolysis, only hydrogen is released as a gaseous byproduct; hence, the second product, sodium metaborate, is non-toxic and can be recycled into corresponding borohydride. Despite its potential, NaBH<sub>4</sub> hydrolysis faces significant challenges. In other words, NaBH<sub>4</sub> can undergo self-hydrolysis and subsequently release hydrogen. This process occurs naturally, although the reaction rate is rather slow. The hydrolysis of NaBH<sub>4</sub> for hydrogen generation is kinetically challenging under ambient conditions in the absence of a catalyst. Consequently, considerable efforts have been dedicated to the development of active catalysts to generate a high hydrogen production rate under mild conditions [16, 18]. In this context, noble metal-based catalysts (particularly with Ru [19], Pt [20] and Pd [21]) are particularly efficient. Furthermore, non-precious metal-based materials are a propitiate alternative, among which cobalt [22], nickel [23], and iron [24], revealing catalysts are the most promising. Although catalysts based on metals such as Fe, Cu, Co, and Ni, which are cost-affordable, possess promising catalytic activity. In the present work, we report the consequences of green synthesis of Co<sub>3</sub>O<sub>4</sub> NPs by parsley extract via microwave method. Phase formation, particle size, and surface features have been investigated utilizing a variety of integrated physicochemical tools. Moreover, the activity of these Co<sub>3</sub>O<sub>4</sub> NPs was evaluated towards the hydrolysis of NaBH<sub>4</sub> at 30-45 °C. Furthermore, the investigation was extended to examine the catalytic performance by varying the reaction conditions such as the weight of catalyst, weight of NaBH<sub>4</sub>, alkalinity effects, recyclability of the catalyst.

# 2. Experimental procedures

#### 2.1. Materials

All chemical substances utilized during synthesis and catalytic measurements were purchased from commercial sources without any purification. Cobalt(II) nitrate (Co(NO<sub>3</sub>)<sub>2</sub>·6H<sub>2</sub>O, Alpha Chemika, purity 99%), sodium borohydride (NaBH<sub>4</sub>, SDFCL, purity 98%), ammonium hydroxide (NH<sub>4</sub>OH, Alpha chemicals, concentration of approximately 33%), and sodium hydroxide (NaOH, PIOCHEM, purity 99%). For the preparation of solutions, distilled water was utilized.

#### 2.2. Synthesis of Co<sub>3</sub>O<sub>4</sub> NPs

The green source, parsley plant employed in the present investigation, was purchased from the local market in Sohag city. The synthetic process of parsley extract can be summarized as follows. Firstly, 100 g of fresh parsley plant was washed with tap water followed by distilled water to remove any adsorbed impurities such as contaminants and dust. For finely cutting parsley plants, a Moulinex chopper was used for 2 minutes to

give more interaction during the synthesis approach. The chopped plant was transferred into a round flask containing 400 mL of distilled water and then refluxed at 90 °C for 1 hour. Finally, the obtained extract was cooled and filtered by utilizing the Whatman filter paper.

For the green synthesis of Co<sub>3</sub>O<sub>4</sub> NPs, 15 g of cobalt nitrate was dissolved in 50 mL of distilled water and then transferred into a beaker containing 300 mL of parsley extract. The extract solution color was changed rapidly from yellow to red. Subsequently, the mixture was stirred, and its pH value was adjusted to 9 by the drop-wise addition of ammonia (1:1) until the red color of the solution changed to a green color. Subsequently, the obtained precipitation was exposed to microwave irradiation for 8 minutes at 600 W. The precipitate obtained after the microwave irradiation was washed many times with distilled water, filtered by using Whatman filter paper then dried in a drying oven at 80 °C overnight. In a porcelain crucible, the dried powder was calcined in a muffle furnace at 400 °C for 12 hours (heating rate 1 °C min<sup>-1</sup>) under air flow. Finally, the yield was homogenized utilizing a mortar, and the obtained fine black powder was kept in an Eppendorf tube. The various steps involved during the synthesis of Co<sub>3</sub>O<sub>4</sub> NPs utilizing parsley extract and microwave irradiation method are schematically presented in Fig. 1.

#### 2.3. Instruments for characterization

The phase information about the crystal structure of the synthesized catalyst was examined by utilizing X-ray diffraction (XRD) on a Bruker diffractometer (model D8). The operating XRD operating parameters were Cu- $K_{\alpha}$  radiation ( $\lambda = 1.5418 \text{ Å}$ ) and scan rate of  $0.05^{\circ}$  min<sup>-1</sup> over  $2\theta$  range of  $15^{\circ}$ -80°. For investigating the functional groups in the prepared nanoparticles, Fourier-transform infrared (FT-IR) spectroscopy was analyzed over the wavenumber range 4000-400 cm<sup>-1</sup> on Bruker FT-IR apparatus (model Alpha) using the KBr methodology. The morphology and size of nanoparticles were obtained from the JEOL high-resolution transmission electron microscope (HR-TEM), model JEM-2100F, which was operated at 200 kV. To examine the texture of Co<sub>3</sub>O<sub>4</sub> NPs, a Quantachrome gas sorption instrument (model NOVA 3200) was utilized for constructing the N2-adsorption isotherm of the formed catalyst at -196 °C. Examining the surface chemical composition of the present catalyst was performed X-ray photoelectron spectroscopy (XPS) on Thermo Fisher instrument (model K-Alpha). The operation conditions monochromatic Al K<sub>α</sub> X-ray radiation, spot size 400 μm, binding energy (BE) range of 0 to 1347.8 eV, and pressure of  $5\times$ 10<sup>-10</sup> mbar.

# 2.4. Catalytic activity assessment

The catalytic activity measurements were conducted using a gasometric apparatus similar to a closed-glass apparatus previously reported by Deren' et al. [25]. The apparatus consists of a 100 ml reaction flask connected to a glycerin manometer and two burettes (50 and 100 mL) filled with distilled water. The reaction flask is placed into 1 L beaker on digital hotplate, which

**Eq. 5** 

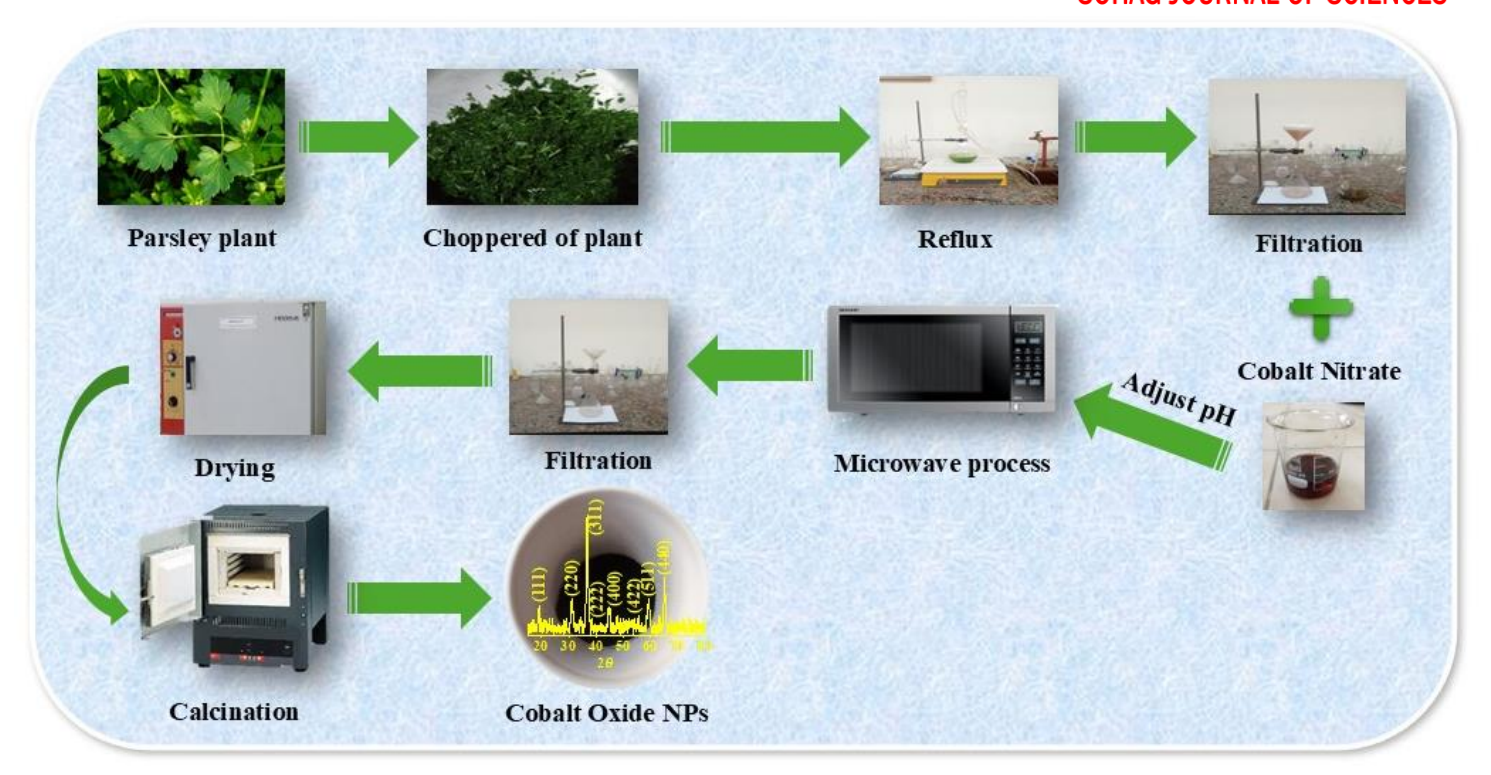


Fig. 1. Schematic of synthesis Co<sub>3</sub>O<sub>4</sub> NPs by using parsley extract via microwave approach. temperature was adjusted by a contact thermometer. During NaBH<sub>4</sub> hydrolysis, the volume of H<sub>2</sub> evolution was measured by the displacement of water and recorded as a function of time. For each measurement, the catalytic reaction flask was connected to the glass apparatus containing 10 mg of the catalyst and 20 ml of a NaBH<sub>4</sub> solution (0.75 wt.%). The catalytic reaction was evaluated at temperatures of 30, 35, 40, and 45 °C. Other parameters have been examined too, which involve the catalyst weight, NaBH<sub>4</sub> concentrations, the effect of alkalinity, and the recycling of the synthesized catalyst. The hydrogen generation rate (HGR) was calculated by utilizing Equation 2:

HGR (ml.g<sup>-1</sup>.min<sup>-1</sup>) = 
$$\frac{V_{H_2} (ml)}{t (min) * Wt.cat.(g)}$$
 Eq. 2

Calculating the thermodynamic parameters for the catalytic reaction was performed using the Arrhenius and Eyring equations 3 and 4:

$$\ln (k) = \ln (A) + \frac{E_a}{RT}$$
 Eq. 3

In Arrhenius equation, k is the reaction rate constant, A is the Arrhenius constant, Ea is an activation energy, R is a gas constant, and T is the absolute temperature of the reaction in Kelvin.

$$\ln\left(\frac{kh}{k_BT}\right) = \frac{-\Delta H^*}{RT} + \frac{\Delta S^*}{R}$$
 Eq. 4

where k refers to the rate constant, h is a Planck constant, k<sub>B</sub> is a Boltzmann constant, T is the absolute reaction temperature in Kelvin, H\* refers to the standard enthalpy of activation, S\* is the standard entropy of activation, and R is the universal gas constant. Additionally, the Gibbs energy of activation ( $\Delta G^*$ ) can be calculated using equation 5:

$$\Delta G^* = \Delta H^* - T\Delta S^*$$

3. Results and Discussion:

# 3.1. Characterization

#### 3.1.1. Phase identification

Fig. 2(a) shows the XRD pattern of Co<sub>3</sub>O<sub>4</sub> NPs synthesized by the green route via the microwave approach. Seven diffraction peaks can be seen at  $2\theta = 19.18^{\circ}$ ,  $31.40^{\circ}$ ,  $37.04^{\circ}$ ,  $38.86^{\circ}$ ,  $44.88^{\circ}$ , 59.58°, and 65.50°. These peaks could be ascribed to the (111), (220), (311), (222), (400), (511), and (440) planes of the facecentered cubic Co<sub>3</sub>O<sub>4</sub> spinel (JCPDS file No. 03-065-3103, lattice constant a = 8.056Å, and space group Fd-3m), respectively. Moreover, the diffractogram of Co<sub>3</sub>O<sub>4</sub> NPs reveals the absence of any reflections attributable to other cobalt oxide phases such as CoO or Co<sub>2</sub>O<sub>3</sub>. Table 1 lists all detected reflections of Co<sub>3</sub>O<sub>4</sub> spinel and their standard JCPDS values of  $2\theta$  and d-spacing. The values of  $2\theta$  and d-spacing well matched with the values in the standard JCPDS card. The average crystallite size of Co<sub>3</sub>O<sub>4</sub> NPs was estimated to be equal to 15 nm by utilizing the Scherrer equation (Equation 6).

$$D = \frac{k \lambda}{\beta \cos \theta}$$
 Eq. 6

where D is grain size, k = 0.9 is Scherrer constant,  $\lambda$  is the X-ray wavelength,  $\beta$  is the FWHM (in radians),  $\theta$  is the diffraction angle.

The FT-IR spectrum of the obtained Co<sub>3</sub>O<sub>4</sub> NPs after calcination at 400 °C exhibits various absorption peaks at wavenumber ranges between 4000-400 cm<sup>-1</sup> as shown in Figure 2(b). The broad absorption peak at 3386 cm<sup>-1</sup> is attributed to the O-H stretching vibration that corresponds to the adsorbed H<sub>2</sub>O

# **Research Article**

molecules [26, 27]. The two peaks at 2967 cm<sup>-1</sup> and 2859 cm<sup>-1</sup> could be indexed to symmetric and asymmetric aliphatic stretching of C-H vibrations, respectively [26, 27]. Two bands are located at 1632 cm<sup>-1</sup> and 1384 cm<sup>-1</sup> due to stretching modes of the carboxylic group (asymmetric and symmetric mode of (-COO-), respectively [26, 28, 29]. Moreover, the absorption peak at 1632 cm<sup>-1</sup> could be assigned to the bending vibration mode of H-O-H. Weak bands at 905 cm<sup>-1</sup> and 804 cm<sup>-1</sup> correspond to the stretching vibrations of C-O in carbonate species as asymmetric stretching, and bending vibration, respectively [30]. More obviously, the FT-IR spectrum displays two sharp absorption bands at 666 cm<sup>-1</sup> and 570 cm<sup>-1</sup> that confirmed the formation of Co<sub>3</sub>O<sub>4</sub> NPs. The first peak at 666 cm<sup>-1</sup> is assigned to Co<sup>2+</sup> vibrations at a tetrahedral site that corresponds to the stretch vibration of O-Co-O [31, 32]. The other peak at 570 cm<sup>-1</sup> is attributed to Co3+ vibration on an octahedral site that corresponds to the stretch of Co-O [33, 34]. The XRD and FT-IR findings are straightforward evidence for the development of biosynthesis of Co<sub>3</sub>O<sub>4</sub> spinel.

**Table 1.** Standard XRD JCPD data (card No. 03-065-3103) and those of the synthesized catalyst.

JCPDS values		Synthesized Co <sub>3</sub> O <sub>4</sub>			
2θ, (deg.)	d-spacing, (Å)	(hkl)	2θ, (deg.)	d-spacing, (Å)	
19.07	4.65	(111)	19.18	4.63	
31.38	2.85	(220)	31.40	2.85	
36.98	2.43	(311)	37.04	2.43	
38.69	2.33	(222)	38.86	2.32	
44.97	2.01	(400)	44.88	2.02	
59.59	1.55	(511)	59.58	1.55	
65.5	1.42	(440)	65.50	1.43	

#### 3.1.2. Morphology inspection

To reveal the NPs morphology, HR-TEM was utilized to obtain more information about the shape and size of obtained Co<sub>3</sub>O<sub>4</sub> NPs as shown in Figure 3. In HR-TEM images, Co<sub>3</sub>O<sub>4</sub> NPs are observed in a network of agglomerated NPs with an obvious porosity (Fig. 3(a)). The magnified part clearly reveals the synthesized Co<sub>3</sub>O<sub>4</sub> NPs possess nano-capsules morphology (Fig. 3(b)). The SAED patterns demonstrate significant superimposed bright ring patterns that confirm the crystallinity of Co<sub>3</sub>O<sub>4</sub> NPs (Fig. 3(c)). In Figure 3(d) through calculating around 11 particles, the obtained average particle size of NPs is approximately 10 nm.

#### 3.1.3. Surface assessment

The textural properties of the obtained catalyst were examined by  $N_2$  physisorption measurements. The  $N_2$  adsorption-desorption isotherm and pore size distribution pattern by the

DFT method is revealed in Figure 4. The obtained isotherm (Figure 4(a)) exhibits a mixture of Type II and Type IV characters according to the IUPAC classification [35].

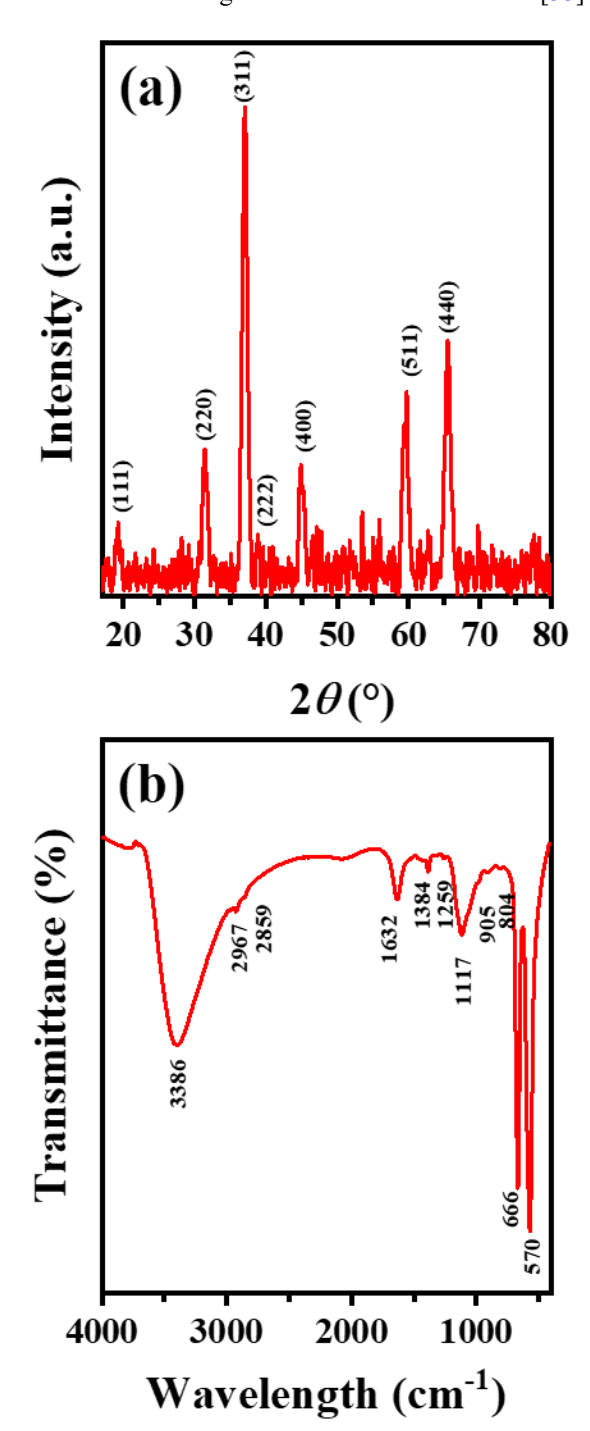


**Fig. 2.** X-ray diffraction pattern (a) and FT-IR spectrum (b) of the synthesized Co<sub>3</sub>O<sub>4</sub> NPs

At high relative pressure, the absorbed volume increases with the thickness of an adsorbed layer until P/Po = 1. The hysteresis loop type H3 of isotherm has appeared at P/Po = 0.7, which aggregates as plate-like particles forming slit-like pores. The computed specific surface area of the obtained Co<sub>3</sub>O<sub>4</sub> NPs using the BET method,  $S_{\rm BET}$ , was found to be 90 m²  $g^{-1}$ .

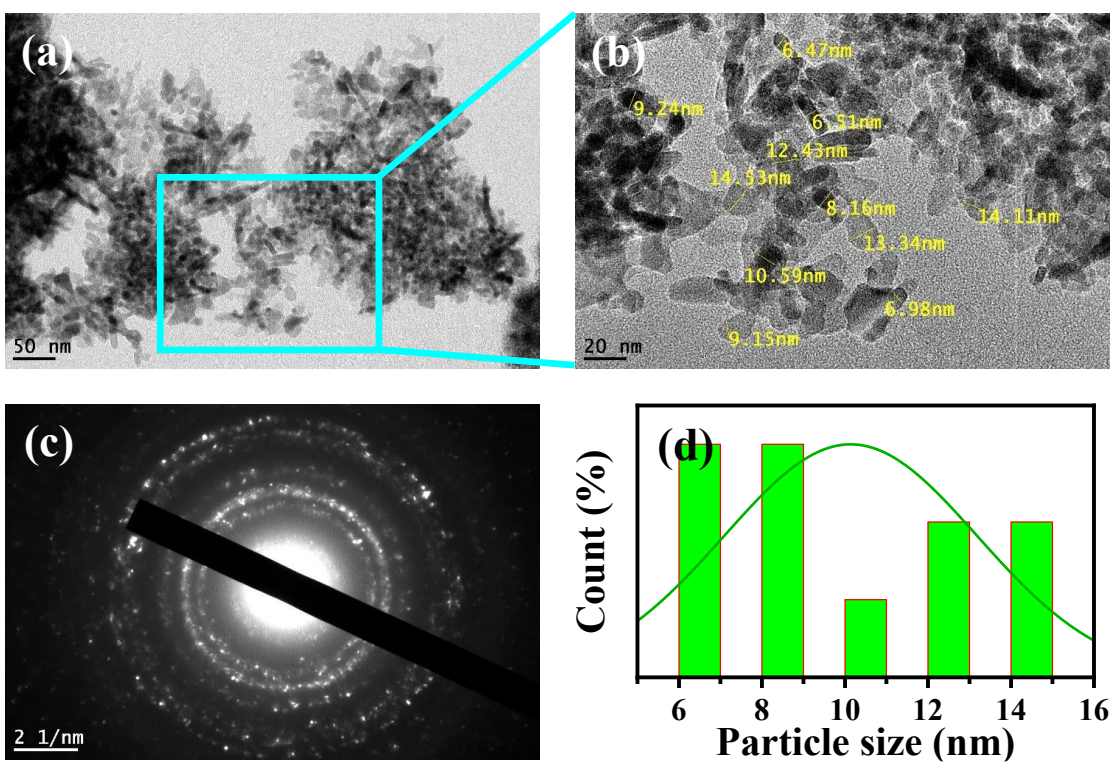


Fig. 3. TEM images (a)and (b), SAED pattern(c), and average particle sizes (d) of the synthesized Co<sub>3</sub>O<sub>4</sub> NPs.

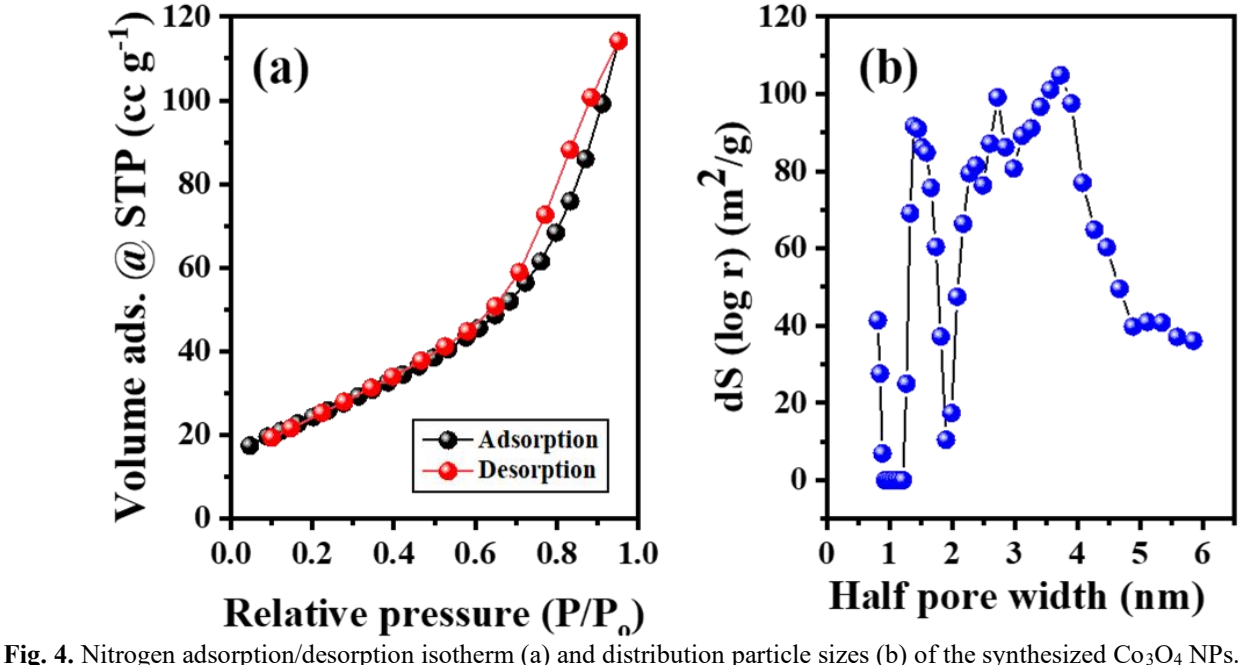


Fig. 4. Nitrogen adsorption/desorption isotherm (a) and distributed This value is much higher than that, 19 m<sup>2</sup> g<sup>-1</sup>, reported for Co<sub>3</sub>O<sub>4</sub>/C nanocomposite calcined at 400 °C. which was prepared by the green method using basil leaves extract [36]. Moreover, it is extremely larger than those reported for the recently reported values for the green-synthesized Co<sub>3</sub>O<sub>4</sub> NPs employing jasmine flowers extract and subsequent calcination at 300 °C (6 m<sup>2</sup> g<sup>-1</sup>) and 500 °C (2 m<sup>2</sup> g<sup>-1</sup>) [37]. These findings highlight the role of the green precursor in controlling the texture of the prepared nanomaterials. By utilizing the DFT method, the

particle size distribution was plotted as shown in Figure 4(b). Inspection of the obtained distribution reveals the presence of poly-disperse character. The first peak can be seen at pore width of approximately 3 nm, which is in the vicinity of the microporous region. Another wide-peak lying in the mesoporous range composed of three maxima at pore widths of 3.5, 4.5, and 7.5 nm.

XPS analysis of synthesized  ${\rm Co_3O_4\,NPs}$  was utilized to estimate the chemical composition and valance state of the elements at

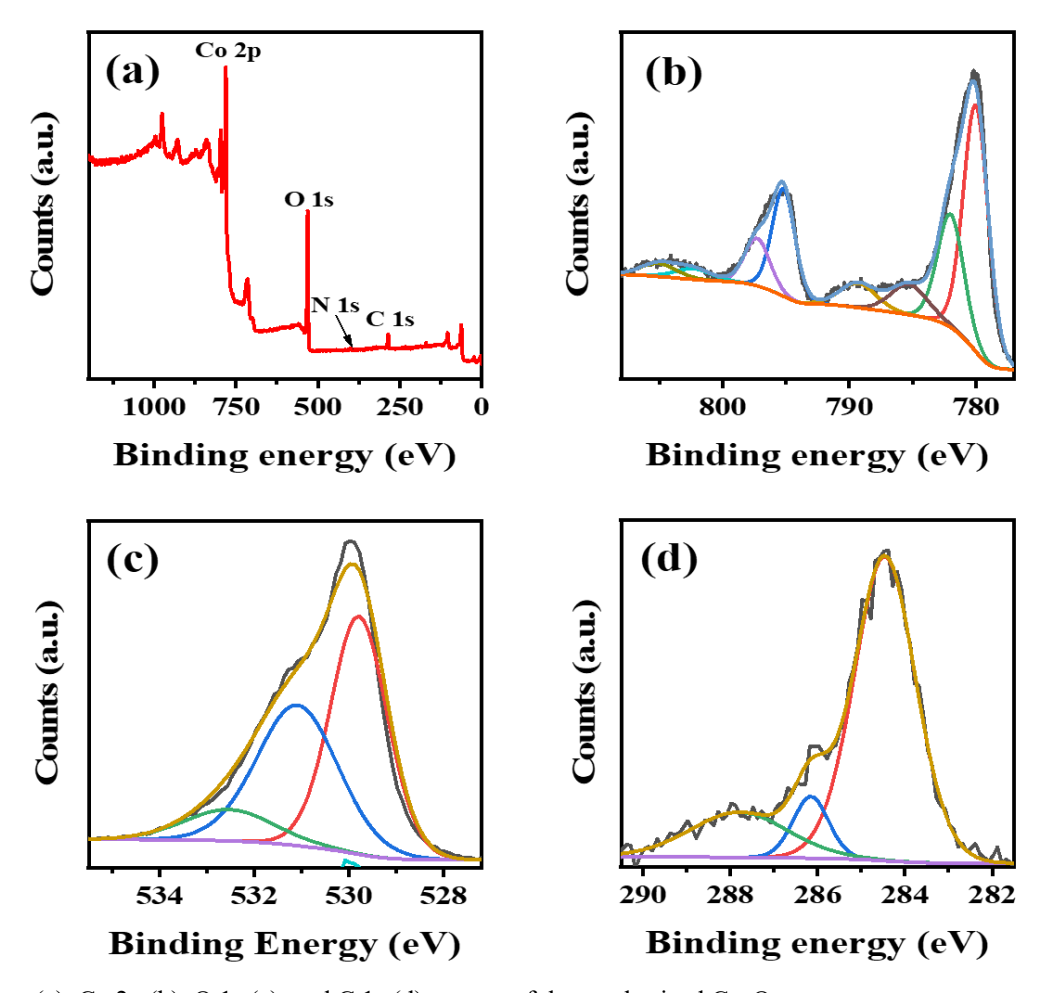


Fig. 5. XPS survey (a), Co 2p (b), O 1s (c), and C 1s (d) spectra of the synthesized Co<sub>3</sub>O<sub>4</sub>.

the surface of the obtained catalyst. In Fig. 5(a), the survey spectrum demonstrates the presence of Co, O, C, and N elements on the surface of the present sample. The presence of both Co and O elements is expected for the synthesized Co<sub>3</sub>O<sub>4</sub>, whereas the C and N ones could arise from the phytochemicals present in the parsley extract that adhere to the surface of Co<sub>3</sub>O<sub>4</sub> nanoparticles, functioning as stabilizing and capping agents. The XPS surface concentrations of Co, O, C, and N elements are 31.72 %, 50.83 %, 16.64 %, and 0.81 %, respectively. As can be seen in Figure 5(b), the Co 2p spectrum shows two asymmetric broad peaks at the binding energy (BE) values of approximately 780.96 and 794.83eV that could be correlated to Co 2p<sub>3/2</sub> and Co 2p<sub>1/2</sub> electronic levels, respectively [36-38]. Similar information could be abstracted from the deconvolution of both levels (Fig. 5(b)). Therefore, we will focus on the fitting of Co 2p<sub>3/2</sub> electronic level only. Two valance states of the cobalt element in the prepared catalyst can be identified in the fitted Co 2p<sub>3/2</sub>, viz. Co<sup>3+</sup> and Co<sup>2+</sup>, which could be correlated with the peaks at BEs of 779.78 and 780.96 eV, respectively [36-38]. The other two peaks at BEs of 785.29 and 789.32 eV are attributed to the Co shake-up satellite peaks [36-39]. The high-resolution O 1s spectrum appear at 526–536 eV, which can be divided into three peaks (Figure 5(c)). These peaks include surface lattice oxygen at 529.84 eV, chemisorbed oxygen in the form of OH groups at 530.86 eV, and adsorbed water and/or carbonate species at 533.47 eV [36, 38, 40-42]. The C 1s fitted XPS spectrum (Fig. 5(d)) displayed three peaks at 284.64 eV (C-C) [43], 287.29 eV (C-N/ C=N) [44], and 288.57 eV (C=O) [45], probably originating from the decomposition residue of the phytochemical in the green source [36, 42-45].

#### 3.2. Catalytic hydrogen generation via NaBH<sub>4</sub> hydrolysis

## 3.2.1. Effect of temperature

Examination of evolved hydrogen gas from catalytic hydrolysis of NaBH<sub>4</sub> with the calcined catalyst at various temperatures (30 – 45 °C). The obtained data were plotted as hydrogen volume versus time as seen in Fig. 6(a). Fig. 6(b) reveals that the computed HGR values increase with the reaction temperature. The catalytic activity increases with elevating temperature due to the expected increase in energetic collisions between the reactants and the active sites on Co<sub>3</sub>O<sub>4</sub> NPs. Moreover, these collisions facilitate an increasing amount of liberated hydrogen molecules through the catalytic reaction leading to higher hydrogen generation rate values. These findings reveal the importance of elaborating the catalytic mechanism between NaBH<sub>4</sub> molecules and Co<sub>3</sub>O<sub>4</sub> NPs.

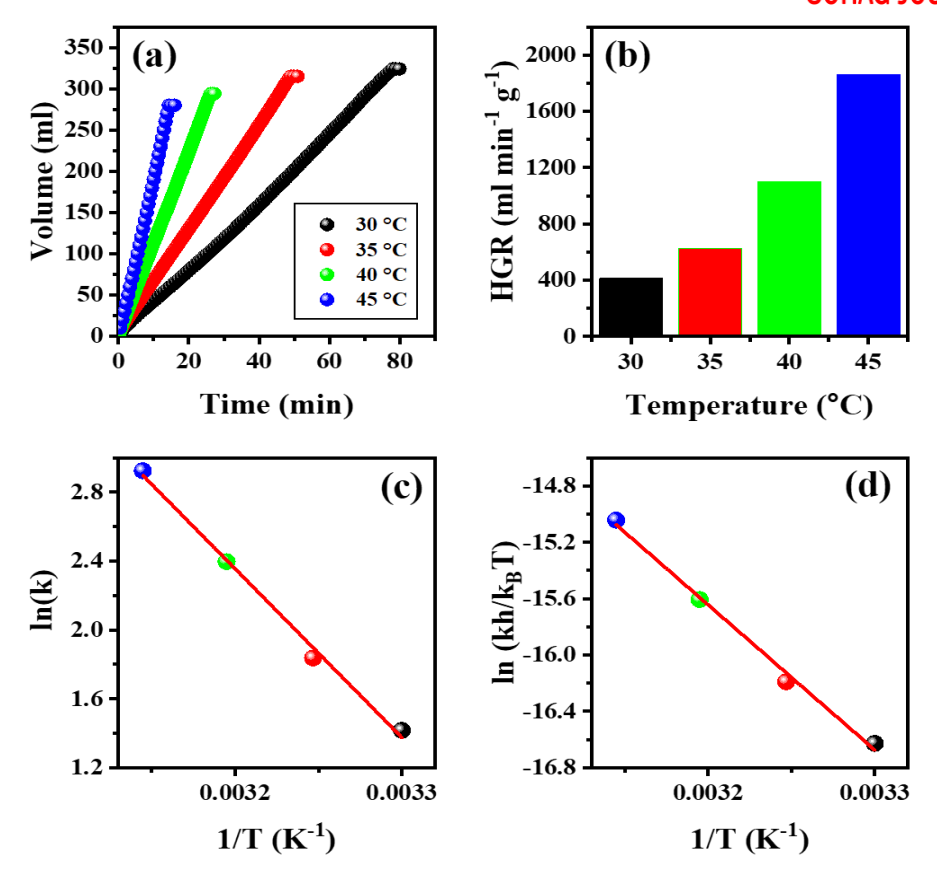


**Fig. 6.**  $V_{H_2}$ -time curves (a), HGR versus reaction temperature (b), Arrhenius plot (c), and Eyring plot (d) abstracted from NaBH<sub>4</sub> hydrolysis over  $Co_3O_4$  NPs.

Langmuir-Hinshelwood mechanism is widely reported for understanding the NaBH<sub>4</sub> hydrolysis over various catalysts showing the maximum HGR value of 1863 ml.g <sup>-1</sup>.min<sup>-1</sup> at 45 °C. The mechanism that the reaction initiated by the adsorption of BH<sub>4</sub> and H<sub>2</sub>O molecules on the cobalt-based catalyst surface [22, 36, 37]. It is believed that Co<sup>2+</sup> (electron rich) and Co<sup>3+</sup> (electron deficient) are the adsorption sites for these two reactants, respectively [22, 36, 37]. In a second step, hydride ion (from adsorbed BH<sub>4</sub>-) interacts with H atom (from adsorbed H<sub>2</sub>O) liberating one H<sub>2</sub> molecule. This is accompanied by a transformation of the adsorbed OH ion to BH<sub>3</sub> forming another adsorbed species, i.e. BH<sub>3</sub>(OH)<sup>-</sup>. By repeating this step three times, the final products are 4 H<sub>2</sub> molecules and B(OH)<sub>4</sub> as a by-product [46] according to:

$$BH_3(OH)^- \rightarrow BH_2(OH)_2^- \rightarrow BH(OH)_3^- \rightarrow B(OH)_4^-$$

The XPS data obtained for this catalyst revealed the coexistence of both Co<sup>2+</sup> and Co<sup>3+</sup> on its surface.

Accordingly, it is plausible to assign these cations as the electron rich and electron deficient centers responsible for the high activity of the present catalyst. In this context, it was reported that the higher concentration of Co<sup>2+</sup> than Co<sup>3+</sup> leads to a less efficient reduction of Co<sup>2+</sup> ions [47]. Arrhenius's plot shows that the activation energy of this reaction was calculated as 81.57 kJ/mol (Fig. 6(c)). The Eyring plot was used for determining the thermodynamic parameters as shown in Fig. 6(d). Table 2

illustrates the hydrolysis reactions, which are endothermic due to the positive value of enthalpy. A comparison of the catalytic performance of several catalysts containing cobalt for hydrogen evolution from NaBH<sub>4</sub> hydrolysis is presented in the following Table 3, demonstrating the superior performance of the synthesized Co<sub>3</sub>O<sub>4</sub> NPs produced through a green synthesis approach. The comparison study shows that the higher performance of the catalyst because it uses a lower concentration of NaBH<sub>4</sub> than the higher concentration used in other catalysts.

**Table 2:** thermodynamic parameters for the hydrolysis of NaBH<sub>4</sub> utilizing green-synthesized of Co<sub>3</sub>O<sub>4</sub> NPs.

T (K)	E <sub>a</sub> (kJ/mol)	A (S-1)	Δ H* (kJ/mol)	Δ S* (kJ/mol)	Δ G* (kJ/mol.K)
303	81.57	4.55*10 <sup>14</sup>	85.65	0.144	42.018
308					41.298
313					40.578
318					39.858

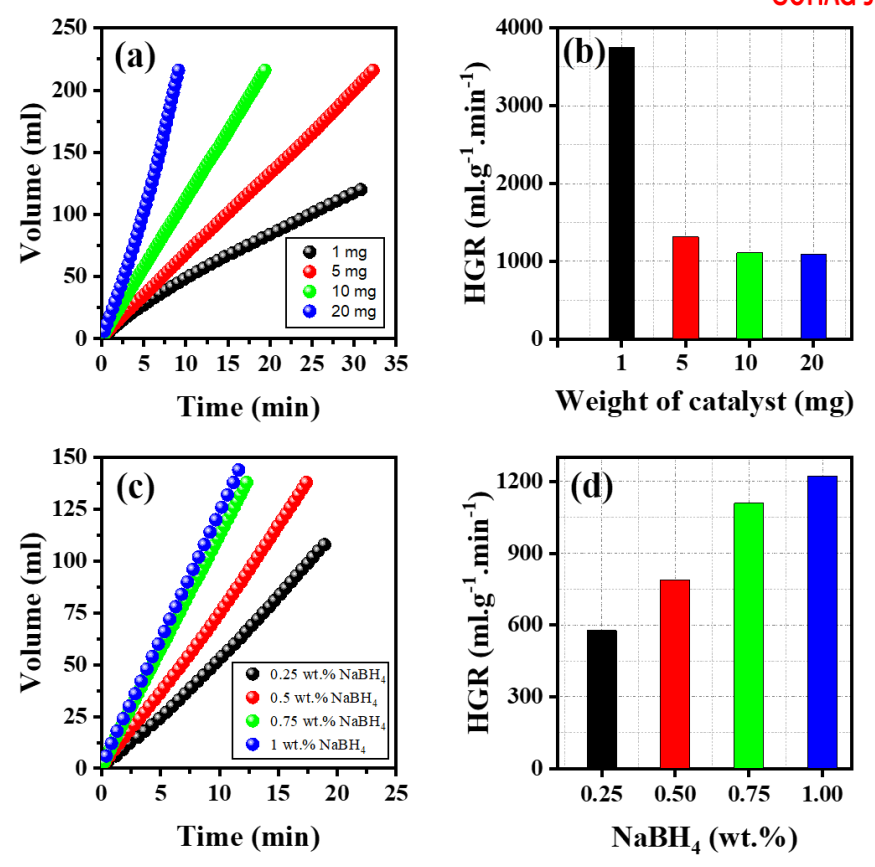


Fig. 7. Effect of catalyst weight (V<sub>H2</sub>-time curves (a) and HGR versus catalyst weight (b)) and NaBH<sub>4</sub> concentration (V<sub>H2</sub>-time curves (c) and HGR versus NaBH<sub>4</sub> concentration (d)) on hydrogen generation over Co<sub>3</sub>O<sub>4</sub> NPs.

#### 3.2.2. Experimental parameters

The crucial parameters utilized to examine their effects on the hydrolysis of NaBH<sub>4</sub> comprise the weight of the catalyst used, various NaBH<sub>4</sub> concentrations, presence of alkali hydroxide, and recyclability. Fig. 7(a) revealed the volume of liberated hydrogen during NaBH<sub>4</sub> hydrolysis with increasing the quantity of the catalyst. Moreover, the HGR is directly affected by the weight of the utilized catalyst (Fig. 7(b)). The impact of catalyst dosage was carried out by varying the catalyst amount from 1 to 20 mg using 150 mg of NaBH4 at 40 °C. The HGR value declined from 3751 to 1089 ml.g -1.min-1. The volume of hydrogen generation was 120 mL in 30.8 min with the reaction conditions 1 mg catalyst, and 150 mg NaBH4 at 40 °C, corresponding to the higher rate of 3751 ml.g <sup>-1</sup>.min<sup>-1</sup>. The obtained HGR decrease with the catalyst weight increase probably due to the increase of the active population at constant NaBH<sub>4</sub> concentration.

Fig. 7(c) shows the dependence of the evolved H<sub>2</sub> volume on reaction time at varying NaBH<sub>4</sub> concentrations (0.25 wt.%, 0.5 wt.%, 0.75 wt.%, and 1 wt.%). The corresponding HGR values are presented in Fig. 7(d). The experiments have been performed using a catalyst amount of 10 mg, and reaction temperature of 40 °C. The data obtained clearly manifest that increasing the concentration of NaBH<sub>4</sub> from 0.25 to 1 wt.% leads to the HGR value increased from 577 to 1223 ml.g <sup>-1</sup>.min<sup>-1</sup>.

**Table 3:** Comparison via catalysts used for NaBH<sub>4</sub> hydrolysis.

Catalyst	Conditions	HGR (ml.g <sup>-1</sup> . min <sup>-1</sup> )	Ref.
Co/Graphene	0.2 wt.% NaBH <sub>4</sub> , 30 °C	188	[57]
Co/γ-Al <sub>2</sub> O <sub>3</sub>	5 wt.% NaBH <sub>4</sub> , 30 °C	220	[56]
Co-La-Zr-B	5 wt.% NaBH <sub>4</sub> , 2 wt.% NaOH, 40 °C	283	[54]
Co/Ni/MWAC	5 wt.% NaBH4, 30 °C	740	[55]
Co <sub>3</sub> O <sub>4</sub> on (Chitosan/urea)	2 wt.% NaBH <sub>4</sub> , 25 °C	1497	[58]
Co <sub>3</sub> O <sub>4</sub> by microwave approach	0.75 wt.% NaBH4, 30 °C	412	This work
Co <sub>3</sub> O <sub>4</sub> by microwave approach	0.75 wt.% NaBH4, 45 °C	1863	This work

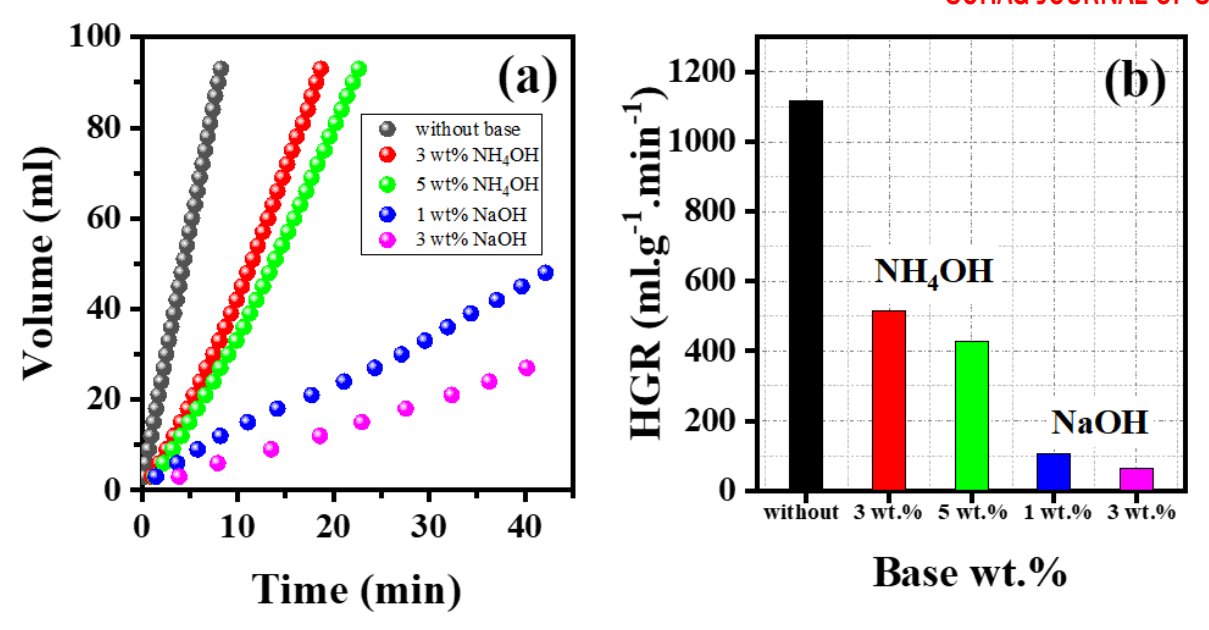


Fig. 8.  $V_{H_2}$ -time curves (a) and HGR versus base concentrations (b) for the hydrogen generation over  $Co_3O_4$  NPs in the presence of NaOH and NH<sub>4</sub>OH.

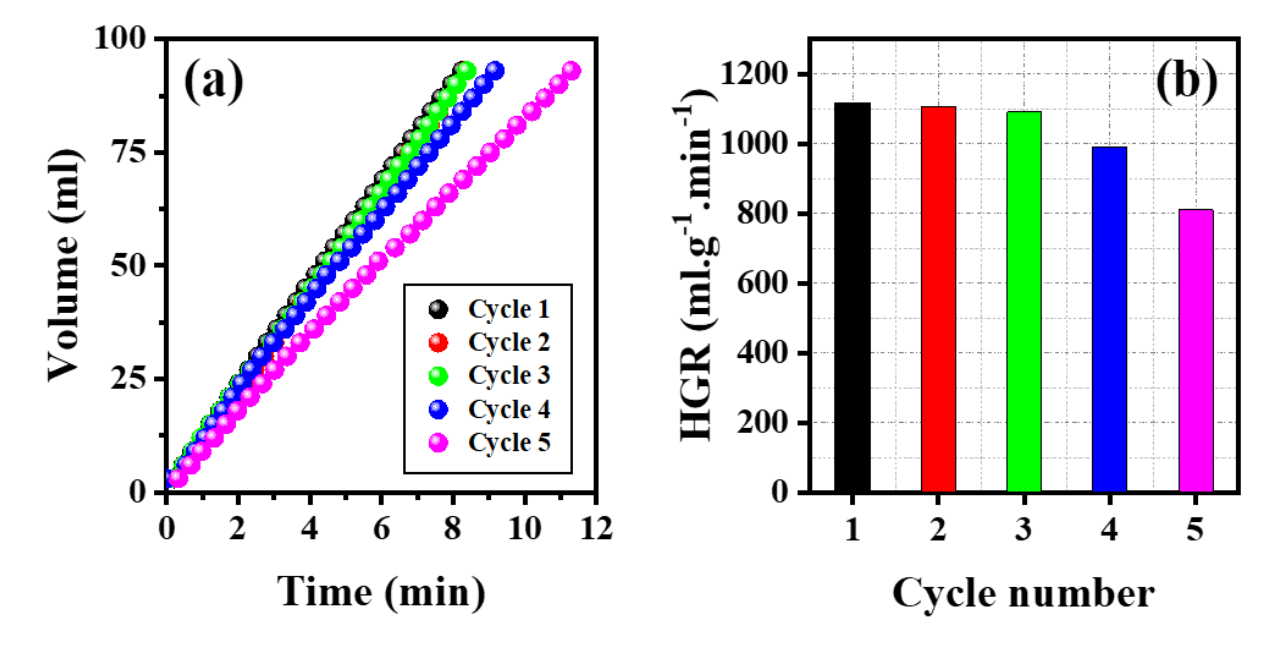


Fig. 9.  $V_{H_2}$ -time curves (a) and HGR versus cycle number (b) obtained from the recycling experiments during NaBH<sub>4</sub> hydrolysis over  $Co_3O_4$  NPs.

These findings show the significant impact of catalyst weight and NaBH<sub>4</sub> concentrations on the catalytic performance of NaBH<sub>4</sub> hydrolysis, which agree with the reported results for this reaction over various cobalt-based catalysts [22, 36, 37, 48, 49].

To inhibit the self-hydrolysis of NaBH<sub>4</sub>, an alkaline medium such as NaOH was used to ensure the stability of the solution during storage [50]. For evaluating this effect, the experiments have been conducted in the presence of two hydroxides (NaOH, NH<sub>4</sub>OH) with two concentrations. The results obtained are presented in Fig. 8 as NaOH concentration increased from 1 to

3 wt.%, the reaction rate (HGR) declined in higher amounts of NaOH. As shown in Figure 8(b), the obtained HGR over the bare catalyst is 1119 ml.g <sup>-1</sup>.min<sup>-1</sup>. Performing the experiment in the presence of 1 wt.% of NH<sub>4</sub>OH is associated with a decline in the activity to 516 ml.g <sup>-1</sup>.min<sup>-1</sup>. A very sharp drop occurs in the presence of 3 wt.% NaOH, which yields HGR value of 106 ml.g <sup>-1</sup>.min<sup>-1</sup>. Further decrease in the HGR values was obtained using higher concentrations of these two bases (Fig. 8(b)). In agreement, Demirci et al. [51] illustrated the effect of increasing NaOH concentrations that declined hydrogen generation rate in

## **Research Article**

continuous activity. The reason for this activity decreases is that the solution density increases with a high alkalinity medium. Subsequently, OH<sup>-</sup> ions can hinder the hydrolysis reaction by decreasing the solubility of NaBO<sub>2</sub>, which can occupy the active sites of the obtained catalyst on the surface leading to a reduction of the catalytic activity [52].

## 3.2.3. Reusability and stability

The reusability of the catalyst is a crucial parameter to assess the catalyst's stability. This is due to ascertaining sustainability for long-term hydrogen generation. The recyclability was investigated by reusing the catalyst for five cycles of hydrogen production at 40 °C under constant operating conditions (10 mg catalyst and 0.75 wt. % NaBH<sub>4</sub>). At the end of each cycle, the utilized catalyst was accumulated using filter paper. After that, the catalyst was washed with distilled water and dried at room temperature. As shown in Fig. 9, the efficiency of NaBH<sub>4</sub> catalytic hydrolysis declined after each run, but the catalyst remained efficient after four consecutive cycles. After completing the 5th cycle, the hydrogen generation rate decreased from 1118.6 to 810.8 ml.g <sup>-1</sup>.min<sup>-1</sup>. The activity of the Co<sub>3</sub>O<sub>4</sub> catalyst in hydrolysis of NaBH<sub>4</sub> decreased to approximately 72% after 5 runs. In each cycle, the degradation of the catalyst performance over time occurred because of the blockage of active sites, and the presence of inactive species on the surface [53]. While repeating hydrolysis cycles, sodium metaborate (NaBO<sub>2</sub>) as a by-product could be adsorbed or precipitated, thus, blocking the active sites on the catalyst surface [48, 49]. Therefore, these findings indicated that the reason for reducing the activity performance of the catalyst is to increase the number of runs.

#### 4. Conclusions

In this study, the purpose was to synthesize a cost-effective catalyst by green route with high catalytic activity to generate hydrogen from NaBH<sub>4</sub> hydrolysis. An efficient catalyst was synthesized by microwave approach using parsley extract as a green source. The standard cubic structure of Co<sub>3</sub>O<sub>4</sub> NPs was confirmed by XRD analysis, which showed an average crystallite size of 15 nm. The morphology of Co<sub>3</sub>O<sub>4</sub> NPs was estimated using TEM images, revealing agglomerated capsules. Whereas FT-IR and XPS demonstrated functional groups and the fundamental composition of the catalyst, respectively. The catalyst illustrated high catalytic performance for NaBH<sub>4</sub> hydrolysis as 1863 ml.g<sup>-1</sup>.min<sup>-1</sup> which was obtained by using the Co<sub>3</sub>O<sub>4</sub> catalyst at 45 °C. The capsule shapes and the high surface area of the synthesized catalyst may be responsible for its maximum hydrogen generation rate. The Co<sub>3</sub>O<sub>4</sub> catalyst's stability and recyclability experiments verified that it remained active and efficient through the fifth cycle.

## **CRediT** authorship contribution statement:

Conceptualization, Tarek T. Ali and Simon W. Samouel; methodology, Simon W. Samouel; software, Hatem A. Mahmoud.; validation, Tarek T. Ali., Bahaa M. Abu-Zied. and Simon W. Samouel; formal analysis, Hatem A. Mahmoud.; investigation, Simon W. Samouel; resources, Bahaa M. Abu-Zied., Hatem A. Mahmoud; data curation, Simon W. Samouel; writing—original draft preparation, Tarek T. Ali., Simon W. Samouel; writing—review and editing, Bahaa M. Abu-Zied., Tarek T. Ali., Hatem A. Mahmoud.; visualization, Bahaa M. Abu-Zied., Hatem A. Mahmoud.; supervision, Tarek T. Ali., Hatem A. Mahmoud., Bahaa M. Abu-Zied. All authors have read and agreed to the published version of the manuscript."

## Data availability statement

The data used to support the findings of this study are available from the corresponding author upon request.

# **Declaration of Competing Interest**

The authors declare that they have no known competing financial interests or personal relationships that could have appeared to influence the work reported in this paper.

# Acknowledgments

The authors express their sincere appreciation to Sohag University for its essential support of this study.

## References

- [1] M. Nilavukkarasi, S. Vijayakumar, S.P. Kumar, Materials Science for Energy Technologies 3 (2020) 371-376.
- [2] X. Zhang, X. Sun, D. Xu, X. Tao, P. Dai, Q. Guo, X. Liu, Applied Surface Science 469 (2019) 764-769.
- [3] I. Mindru, D. Gingasu, L. Patron, A. Ianculescu, V.-A. Surdu, D.C. Culita, S. Preda, C.-D. Negut, O. Oprea, Materials Science and Engineering: B 246 (2019) 42-48.
- [4] J. Ma, A. Manthiram, Rsc Advances 2 (2012) 3187-3189.
- [5] K. Zhou, J. Liu, P. Wen, Y. Hu, Z. Gui, Materials Research Bulletin 67 (2015) 87-93.
- [6] A. Vennela, D. Mangalaraj, N. Muthukumarasamy, S. Agilan, K. Hemalatha, International Journal of Electrochemical Science 14 (2019) 3535-3552.
- [7] M. Khalaj, S.Z. Golkhatmi, A. Sedghi, Diamond and Related Materials 114 (2021) 108313.
- [8] Z. Tang, L. Zhang, S. Tang, J. Li, J. Xu, N. Li, L. Xu, J. Du, Nanomaterials 12 (2022) 2990.
- [9] S. Vijayakumar, A.K. Ponnalagi, S. Nagamuthu, G. Muralidharan, Electrochimica Acta 106 (2013) 500-505.
- [10] B.M. Abu-Zied, T.T. Ali, L. Adly, Catalysis Letters (2024) 1-12.
- [11] X. Xie, Y. Li, Z.-Q. Liu, M. Haruta, W. Shen, Nature 458 (2009) 746-749.
- [12] B.M. Abu-Zied, S.A. Soliman, S.E. Abdellah, Chinese Journal of Catalysis 35 (2014) 1105-1112.
- [13] Z. Cui, Y. Guo, J. Ma, International Journal of Hydrogen Energy 41 (2016) 1592-1599.
- [14] S. Zhironkin, M. Cehlár, Economic and Technological Advances of Green Energy and Sustainable Development: The Overview, vol 16, MDPI, 2023, p. 4193.

- [15] L. Laversenne, C. Goutaudier, R. Chiriac, C. Sigala, B. Bonnetot, Journal of thermal analysis and calorimetry 94 (2008) 785-790.
- [16] J. Shen, D. Xu, J. Ji, Q. Zhang, X. Fan, International Journal of Hydrogen Energy 48 (2023) 1001-1010.
- [17] S.C. Amendola, S.L. Sharp-Goldman, M.S. Janjua, M.T. Kelly, P.J. Petillo, M. Binder, Journal of Power Sources 85 (2000) 186-189.
- [18] H. Al-shaikh, J. Lasri, J.G. Knight, S.T. Al-Goul, Fuel 325 (2022) 124962.
- [19] Y. Tonbul, S. Akbayrak, S. Özkar, Journal of colloid and interface science 513 (2018) 287-294.
- [20] A. Uzundurukan, Y. Devrim, International Journal of Hydrogen Energy 44 (2019) 17586-17594.
- [21] J. Liang, Y. Li, Y. Huang, J. Yang, H. Tang, Z. Wei, P.K. Shen, international journal of hydrogen energy 33 (2008) 4048-4054.
- [22] K. Narasimharao, B.M. Abu-Zied, S.Y. Alfaifi, International Journal of Hydrogen Energy 46 (2021) 6404-6418.
- [23] C. Wu, Y. Bai, D.-X. Liu, F. Wu, M.-L. Pang, B.-L. Yi, Catalysis today 170 (2011) 33-39.
- [24] D. Prasad, K.N. Patil, N. Sandhya, C. Chaitra, J.T. Bhanushali, A.K. Samal, R.S. Keri, A.H. Jadhav, B.M. Nagaraja, Applied Surface Science 489 (2019) 538-551.
- [25] J. Dereń, J. Haber, A. Podgórecka, J. Burzyk, Journal of Catalysis 2 (1963) 161-175.
- [26] R. Atchudan, T.N.J.I. Edison, M. Shanmugam, S. Perumal, T. Somanathan, Y.R. Lee, Physica E: Low-dimensional Systems and Nanostructures 126 (2021) 114417.
- [27] B.M. Abu-Zied, T.T. Ali, L. Adly, International Journal of Hydrogen Energy 48 (2023) 10829-10840.
- [28] T. Seki, K.-Y. Chiang, C.-C. Yu, X. Yu, M. Okuno, J. Hunger, Y. Nagata, M. Bonn, The journal of physical chemistry letters 11 (2020) 8459-8469.
- [29] M. Sabet, K. Mahdavi, Applied surface science 463 (2019) 283-291.
- [30] V. Gruen, S. Kajiyama, S. Rosenfeldt, S. Ludwigs, A.S. Schenk, T. Kato, Crystal Growth & Design 22 (2022) 5883-5894.
- [31] R.V. Narayan, V. Kanniah, A. Dhathathreyan, Journal of Chemical Sciences 118 (2006) 179-184.
- [32] K.P. Latha, C. Prema, S.M. Sundar, Journal of Nanoscience and Technology (2018) 475-477.
- [33] G. Asha, V. Rajeshwari, G. Stephen, S. Gurusamy, D.C.J. Rachel, Materials Today: Proceedings 48 (2022) 486-493.
- [34] S. Farhadi, M. Javanmard, G. Nadri, Acta Chimica Slovenica 63 (2016) 335-343.
- [35] K.S. Sing, Pure and applied chemistry 57 (1985) 603-619.
- [36] B.M. Abu-Zied, K.A. Alamry, Journal of Alloys and Compounds 798 (2019) 820-831.
- [37] E. Hassan, T.T. Ali, B.M. Abu-Zied, Catalysis Letters 155 (2025) 301.
- [38] M. Zhang, M. Xu, H. Hu, J. Qin, S. Zhou, Y. Kong, Journal of Materials Science 57 (2022) 11546-11562.
- [39] B.M. Abu-Zied, M. Alam, A.M. Asiri, J. Ahmed, M.M. Rahman, Microchemical Journal 157 (2020) 104972.

- [40] T.-M. Tien, C.-H. Chen, C.-T. Huang, E.L. Chen, Catalysts 12 (2022) 1474.
- [41] R.K. Devi, G. Muthusankar, S.-M. Chen, G. Gopalakrishnan, Microchimica Acta 188 (2021) 196.
- [42] B.M. Abu-Zied, M.A. Hussein, A. Khan, A.M. Asiri, Materials Chemistry and Physics 213 (2018) 168-176.
- [43] J. Cirone, S.R. Ahmed, P.C. Wood, A. Chen, The Journal of Physical Chemistry C 123 (2019) 9183-9191.
- [44] S. Dou, X. Li, L. Tao, J. Huo, S. Wang, Chemical Communications 52 (2016) 9727-9730.
- [45] V.c.A. de la Peña O' Shea, P.R.r. de la Piscina, N. Homs, G. Aromi, J.L. Fierro, Chemistry of Materials 21 (2009) 5637-5643.
- [46] F. Mirshafiee, M. Rezaei, Scientific Reports 14 (2024) 9659.
- [47] G.N. Glavee, K.J. Klabunde, C.M. Sorensen, G.C. Hadjipanayis, Langmuir 9 (1993) 162-169.
- [48] K. Büyükkanber, A. Ekinci, Ö. Şahin, International Journal of Hydrogen Energy 79 (2024) 335-345.
- [49] A.K. Beheshti, M. Rezaei, S.M. Alavi, E. Akbari, M. Varbar, International Journal of Hydrogen Energy 51 (2024) 661-670.
- [50] R. Kadrekar, N. Patel, A. Arya, Applied Surface Science 518 (2020) 146199.
- [51] U.B. Demirci, P. Miele, Physical Chemistry Chemical Physics 12 (2010) 14651-14665.
- [52] M.S. Keskin, M.S. Ağırtaş, Ionics 29 (2023) 3713-3721.
- [53] F. Abdulaziz, R.R.D. Patel, T.A.M. Taha, Journal of Sol-Gel Science and Technology (2024) 1-13.
- [54] M.H. Loghmani, A.F. Shojaei, Energy 68 (2014) 152-159.
- [55] M. Soltani, M. Zabihi, International Journal of Hydrogen Energy 45 (2020) 12331-12346.
- [56] A. Didehban, M. Zabihi, J.R. Shahrouzi, International Journal of Hydrogen Energy 43 (2018) 20645-20660.
- [57] D. Zhao, Z. Nan, Functional Materials Letters 9 (2016) 1650009
- [58] G.R.M. Tomboc, A.H. Tamboli, H. Kim, Energy 121 (2017) 238-245.